Reactive Scattering from Brute Force Oriented Molecules: K + IR → KI + R (R = *i*-C_3H_7 and *t*-C_4H_9)

H. J. Loesch* and J. Möller

Fakultät für Physik, Universität Bielefeld, Universitätsstrasse 25, D-33615 Bielefeld, Germany

Received: April 8, 1998; In Final Form: June 26, 1998

We report results of a crossed molecular beam study on the reactions K + *i*-C_3H_7I → KI + *i*-C_3H_7 (R1) and K + *t*-C_4H_9I → KI + *t*-C_4H_9 (R2) performed at an elevated collision energy of 1.55 eV for both nonoriented and oriented reagent molecules. Orientation was achieved by using the brute force technique. The most important results are the following: (i) The flux of scattered products of R2 consists of a dominant fast and a minor slow component; the two reaction channels occur with a branching ratio of 100:2. In R1 the fast component only has been observed. (ii) In the center-of-mass frame the dominant component is preferentially scattered into the backward hemisphere with a propensity for sideways and backward scattering while the minor one is sharply forward scattered and travels on the average with the spectator stripping velocity. (iii) The parallel and perpendicular differential steric effects in both R1 and the dominant channel of R2 are very substantial and amount to a size close to the theoretical upper boundary. The parallel steric effect in the minor channel of R2 is rather weak, and the sign is likely to be opposite to the one of the dominant channel. (iv) From the differential steric effects we have deduced the moments J_{10} and J_{11} of an expansion of the orientation-dependent double-differential cross section in a series of real spherical harmonics. (v) Shape and magnitude of the moments are consistent with a tight vector correlation between the directions of the main product flux and the molecular principal *a*-axis. (vi) The steric opacity functions for R1 and the dominant channel of R2 indicate that attacks of the K atoms to the I end of the reagent molecules are favorable for the formation of the fast products. The favored end for the production of the minor component of R2 is likely to be the alkyl group. (vii) The emergence of the minor slow component in R2 has been qualitatively rationalized on the basis of the harpooning mechanism and electronic structure arguments. The model identifies the slow products as KI and electronically excited *t*-C_4H_9.

I. Introduction

The reactions of alkali atoms with alkyl halides have been intensively studied during the "alkali age" of crossed molecular beam kinetics in the 1960s and 1970s.[1−4] The product angular distributions in the center-of-mass (CM) frame at thermal collision energies always featured a preferential scattering of the alkali halides into the opposite direction of the incoming atoms (*rebound* reactions). This characteristic backward scattering could be quantitatively rationalized by the DIPR (direct interaction with product repulsion) model[5] originally formulated to explain the results obtained for the prototype rebound reaction K + CH_3I → KI + CH_3. In a few studies performed at elevated energies, deviations from the characteristic backward scattering have been observed;[3,6,7] however, there are indications that the departures are caused only by the higher stripping velocities that result at these experimental conditions.[8]

The symmetric top molecule methyl iodide is ideally suited for being focussed and oriented in an electric hexapole field. It is for this reason that the systems K and Rb + CH_3I play a key role in the investigation of steric effects.[9−11] It was found at thermal collision energies that products are favorably formed if the alkali atom attacks the molecule from the I end. The methyl group shields the iodine atom very well and creates a cone of nonreaction with a half-angle of around 50°. A study with the (pseudo) symmetric top *t*-butyl iodide showed that the bulkier *t*-butyl group leads to a more marked steric hindrance of the reaction in agreement with chemical intuition.[9] In more recent experiments K + CH_3I has been used as a benchmark system to examine the reliability of the brute force orientation technique.[12] The studies provided experimental evidence for the tight correlation between the directions of the main product flux and the molecular symmetry axis predicted by the harpooning mechanism and the DIPR model.

In this paper we report the results of a crossed molecular beam study on the exoergic reactions

$$\mathrm{K} + i\text{-}\mathrm{C_3H_7I} \rightarrow \mathrm{KI} + i\text{-}\mathrm{C_3H_7} \qquad \Delta D_0^0 = -1.0\ \mathrm{eV} \quad \text{(R1)}$$

$$\mathrm{K} + t\text{-}\mathrm{C_4H_9I} \rightarrow \mathrm{KI} + t\text{-}\mathrm{C_4H_9} \qquad \Delta D_0^0 = -1.13\ \mathrm{eV} \quad \text{(R2)}$$

performed at the mean collision energies E_{tr} = 1.56 (R1) and 1.54 eV (R2). The experiments with nonoriented, directionally isotropic molecules comprise angular and time-of-flight distributions of products from which we deduce contour maps of the double-differential cross section in the CM frame. We find preferred scattering into the backward hemisphere, but deviating from results on K + CH_3I obtained at thermal energies,[1,2] distributed over a wide angular range with a propensity for sideways and backward scattering and an inhibition of forward scattering in accord with earlier results. However, most spectacular and completely unexpected is the conspicuous difference between the two systems: in addition to the flux of fast products common to both systems, R2 exhibits a minor

10.1021/jp9818129 CCC: $15.00
Published on Web 09/02/1998

slow component which appears with a branching ratio of 100:2. This component is sharply forward scattered and travels with a mean velocity amounting exactly to the spectator stripping velocity of R2.

As in our previous work we have oriented the target molecules by using the brute force technique and measured the differential parallel and perpendicular steric effects over a wide range of scattering angles.[13] These quantities are directly related to the first moments J_{10} and J_{11} of an expansion of the orientation-dependent double-differential cross section in a series of real spherical harmonics. They manifest the orientational information accessible under the present operational conditions. Size, sign, and shape of the moments are consistent with a strong vector correlation between the directions of the main product flux and the molecular principal *a*-axis. The steric opacity functions deduced essentially from data obtained for nonoriented molecules indicate that the products of R1 and the fast component of R2 are favorably formed if the K atoms attack the I end of the molecule in agreement with results acquired at thermal and elevated energies for R2 and homologous systems. Steric effects of the minor slow component in R2 are rather weak but they show a propensity for a favorable alkyl end.

In the following section II we describe briefly the apparatus. The experimental data and the contour maps for the scattering from nonoriented molecules are presented in section III. The measured differential parallel and perpendicular steric effects are reported in section IV together with the determination of the moments J_{10} and J_{11}. In the concluding section V we attempt to rationalize the appearance of the minor slow component in R2 on the basis of the harpooning model and electronic structure arguments.

II. Apparatus

For a detailed description of the crossed molecular beam machine we refer to earlier papers.[7,8,12−14] Briefly, two well-collimated, seeded beams of reagent molecules intersect perpendicularly. Their intensities have been monitored by a surface ionization detector (K) or a mass spectrometer (alkyl iodide). Both detection devices have been employed to also measure the beam velocity distributions via standard time-of-flight (TOF) technique. The (density) velocity distributions resulted from fitting the parameters of the function

$$n(v) = \text{const}\cdot v^2 \exp\{-[(v - v_0)/\alpha]^2 \qquad (1)$$

simultaneously to two TOF profiles measured for two different lengths of the flight path. In this way we could determine the absolute velocity with an error below 0.5%. Important dimensions, operation conditions of the beam sources, and velocity parameters are compiled in Table 1.

Both the product molecules KI and the nonreactively scattered K atoms are detected with nearly equal efficiency by surface ionization on a heated Re-ribbon that is accommodated in a separately pumped ultrahigh vacuum chamber. To measure the angular distributions of the scattered particles the detector can be rotated in the plane of the beams around the intersection volume. The product velocity distributions are determined again via standard TOF technique.

Orientation of the molecules is achieved by application of the brute force technique.[13] The electrostatic orientation field E is created by two parallel plates which surround the intersection volume. The field is parallel to the scattering plane and can be rotated by rigidly rotating the plates; its direction is reversed by interchanging the sign of the applied voltages. The directional distribution of the principal *a*-axis of the molecules within the field has been calculated using our computer codes available from an earlier study.[15,16] The computation is based on three assumptions: (i) the rotational state distribution of the beam molecules in the field-free region is governed by a Maxwell−Boltzmann distribution for the rotational temperature T_{rot}, (ii) the molecules behave like rigid bodies, and (iii) the dipole moment of *i*-C_3H_7I is parallel to the *a*-axis. The required molecular constants and brute force parameters are compiled in Table 2. The calculation depends crucially on T_{rot}, but unfortunately, no direct experimental information on the state distribution is available at present. We resort to the upper limit (T_{rot} = 20 K) deduced in section IV.B from the observed field angle dependence of the steric effect and find that the directional distribution of the *a*-axis is well described by the (normalized)

TABLE 1: Important Dimensions, Beam Operation Conditions, and Beam Properties

	K (R1)	K (R2)	*i*-C_3H_7I	*t*-C_4H_9I
beam source				
nozzle diameter (mm)	0.12		0.1	
skimmer diameter (mm)	1.0		0.5	
nozzle−skimmer distance (mm)	15		10	
fwhm of angular beam profile (deg)	1.1		4.8	
stagnation conditions				
vapor pressure (mbar)	3		∼60	
He pressure (mbar)	800		∼900	
nozzle temperature (K)	1050		∼375	
velocity distributions				
flight path (mm)	1133/1433		847/1147	
v_0 (m/s)	2800	2750	1165	1200
α (m/s)	270	260	53	54
$T_{\|\|}$ (K)[a]			28.7	32.3
E_{tr} (eV)	1.56	1.54		
$\|\mathbf{V}\|$ (m/s)	3057	3024		
$\|\mathbf{u}_{strip}\|$ (m/s)	148	182		
product detection				
distance between detector and intersection volume (mm)			490	
flight path (mm)			420	
angular resolving power (deg)				
in plane			0.12	
out of plane			1.2	

[a] Parallel beam temperature calculated from α.

TABLE 2: Molecular Constants and Brute Force Parameters

	i-C_3H_7I[a]	*t*-C_4H_9I[b]	ref
rotational constants (cm^{-1})			
A_0	0.2676	0.1507	27, 28
B_0	0.072 963	0.0521	27, 29
C_0	0.060 63	0.0521	27
dipole moments (debye)			
d_a	1.97	2.13	30
d_b	0	0	
d_c	∼0	0	
C−I bond			
D_0 (eV)	2.30 ± 0.1	2.17 ± 0.1	31
K−I bond			
D_0 (eV)	3.30 ± 0.02		32
brute force parameters			
$\|E\|$ (kV/cm)	20	20	
$\bar{\omega}$	9.9	13.7	33
A_0	0.038[c]	0.041[c]	

[a] The structure is shown in Figure 11 (upper panel). [b] The structure is shown in Figure 11 (lower panel). [c] Deduced from the field angle dependence of the steric effect, Figure 8.

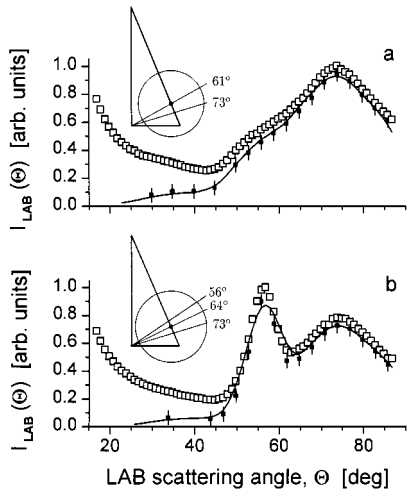

Figure 1. Angular distributions of scattered particles (□) for R1 (panel a) and R2 (panel b). The solid squares mark the distribution of the product intensity alone which has been isolated from the total scattering signal using the TOF profiles. The solid lines are simulations of the reactive scattering based on the results shown in Figure 5a,b.

probability density function

$$\tilde{A}(\cos\theta) = (1/4\pi)(1 - A_0 \cos\theta) \qquad (2)$$

where the orientation parameter A_0 is given in Table 2 and θ denotes the angle between the field E and the direction $\hat{\mathbf{a}}$ of the principal a-axis. $\hat{\mathbf{a}}$ is chosen to be antiparallel to the dipole moment $\mathbf{d}$

$$\hat{\mathbf{a}} = -\hat{\mathbf{d}} \qquad (3)$$

and points exactly along the C−I bond from C to I in t-C_4H_9I and approximately (the angle is ≈12.5°) in i-C_3H_7I. Although correct only for *t*-butyl iodide, we denote hereafter the principal *a*-axis as symmetry axis.

III. Scattering from Nonoriented Molecules

A. Experimental Results. Angular distributions of scattered particles $I_{LAB}(\Theta)$ for R1 and R2 and the corresponding TOF profiles $I_{LAB}(\Theta,t)$ are presented in Figures 1, 2, and 3, respectively. The TOF profiles are normalized such that the area below each curve is proportional to the intensity of the respective angular distribution at the indicated scattering angle Θ.

For both systems the scattering intensity at small angles Θ decreases monotonously with rising Θ up to around 45° (Figure 1). The TOF profiles measured in this region exhibit only one peak. The velocity associated with the peak coincides with the one expected for elastically scattered K atoms and identifies it as being due to elastically scattered K atoms. The elastic intensity gradually decreases with rising Θ and becomes insignificant at large angles. Width and mean velocity of the elastic peaks give no indication for a substantial contribution of deeply inelastic scattered K atoms that would obscure the product flux.

Above Θ = 45° the scattering intensity of R1 grows again (Figure 1a). An inspection of the TOF profiles Figure 2 shows that this rise is caused by the appearance of a somewhat slower contribution whose velocity is well within the range kinematically allowed for the products KI. Therefore, we associate this component with the reaction products KI. The perfect separation of elastic and reactive TOF peaks allows one to eliminate the elastic fraction from the total intensity, and one obtains the distribution of the isolated products given as solid squares in

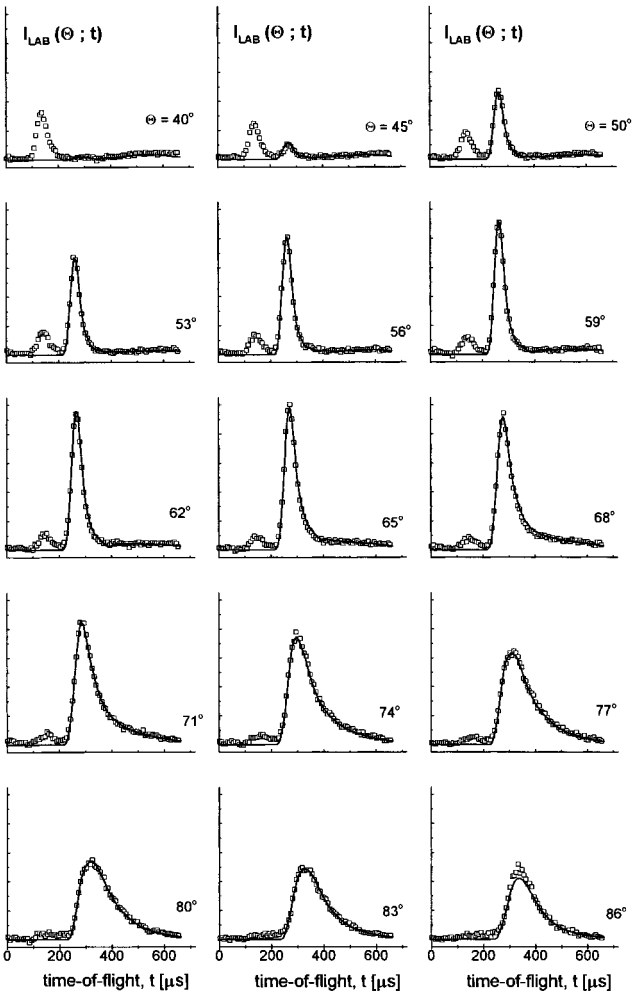

Figure 2. TOF distributions of scattered particles for R1 measured at the indicated LAB scattering angles. The solid lines are simulations based on the results shown in Figure 5a. The structure at small t is due to elastically scattered K atoms; it is not included in the simulation.

Figure 1a. The error bars result from the numerical procedure used for isolating the product intensity which requires integrals over the measured TOF distributions.

The angular distribution for R2 deviates drastically from R1 by a conspicuous peak at intermediate scattering angles (Figure 1b). The TOF profiles (Figure 3) demonstrate that this additional intensity is due to a third peak at large time-of-flights which is present only in a narrow angular range between 50 and 62°. Such a significant difference in the scattering of these two closely related systems was absolutely unexpected; studies at thermal energies performed years ago exhibit no trace of such a phenomenon.[1d] The slow contribution meets all kinematic constraints for KI products and is thus considered as a second component of the KI flux; this identification is supported by further observations mentioned below. The solid squares in Figure 1b represent again the scattering solely of the products.

B. Data Aalysis. The relation between the TOF signal $I_{LAB}(\Theta,t)$ and the double-differential reaction cross section $J_{00}(\vartheta, u)$ in the CM frame is formally given by

$$I_{LAB}(\Theta,t) = K \langle J_{00}(\vartheta, u)\rangle_{\Theta,t} \qquad (4)$$

The variables ϑ and u are the scattering angle and velocity of the detected product in the CM frame. Their relation with the corresponding LAB quantities Θ and V_L is depicted in the kinematic diagram, Figure 4. The bracket $\langle ... \rangle_{\Theta,t}$ symbolizes

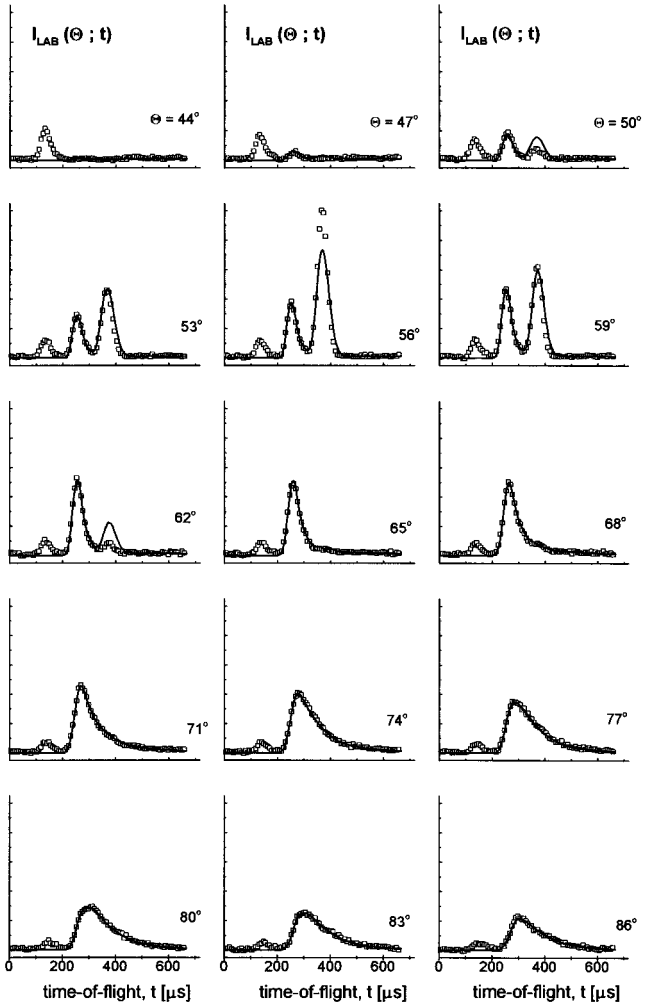

Figure 3. The same as in Figure 2 but for R2. The simulations are based on the results shown in Figure 5b. Note the well-resolved peak at large t between $\Theta = 50°$ and 62°.

the proper transformation of J_{00} into the LAB frame and the integration over the beam velocity distributions and transmission function of the TOF analyzer.[13] To extract J_{00} from the data we employ the fixed velocity approximation (FVA), that is, we ignore the integrations required by the bracket and use instead the mean beam velocities and the nominal time-of-flight. The desired quantity follows then directly from the TOF profiles.[14]

$$J_{00}(\vartheta, u) \approx J_{\mathrm{FVA}}(\vartheta, u) \propto I_{\mathrm{LAB}}(\Theta,t)\, u^2 t^4 \qquad (5)$$

The global cross section $J_{\mathrm{FVA}}(\vartheta,u)$ is obtained by connecting (interpolated) points of equal intensity with contour lines in a polar diagram where ϑ and u are the polar angle and length of the radius vector. The axial symmetry with respect to the relative velocity ($\hat{\mathbf{z}}$-axis) is guaranteed by a reflection of the less noisy points with positive x-component of $\mathbf{u}$ at the $\hat{\mathbf{z}}$-axis. The quality of this approximate procedure is examined by simulating the experimental data on the basis of the FVA contour maps, that is, by performing all integrations included in eq 4 and comparing the simulated with the measured quantities. The advantage of the FVA method over the standard trial and error procedure is that the result is unbiased by the choice of trial functions and the restricting assumption of separable angular and velocity distributions.

Contour maps of the cross section J_{FVA} for both reactions are presented in Figure 5. The solid lines in Figures 1, 2, and

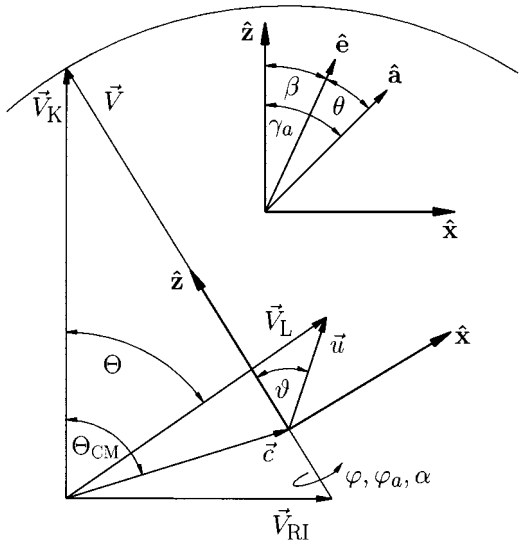

Figure 4. Schematic Newton diagram of the kinematics for R1 and R2. Illustrated is the relation between the velocity $\mathbf{u}$ and scattering angle ϑ of the detected particle in the CM frame $\hat{\mathbf{x}}$, $\hat{\mathbf{y}}$, $\hat{\mathbf{z}}$ and the corresponding quantities $\mathbf{V}_L$, Θ in the LAB frame. The inset defines the polar angles of the orientation field $E = \hat{\mathbf{e}}|E|$ and of the molecular symmetry axis $\hat{\mathbf{a}}$ in the CM frame as well as the angle θ between $\hat{\mathbf{a}}$ and $\hat{\mathbf{e}}$. For clarity the $\hat{\mathbf{y}}$ axis is omitted and the azimuthal angles are shown symbolically.

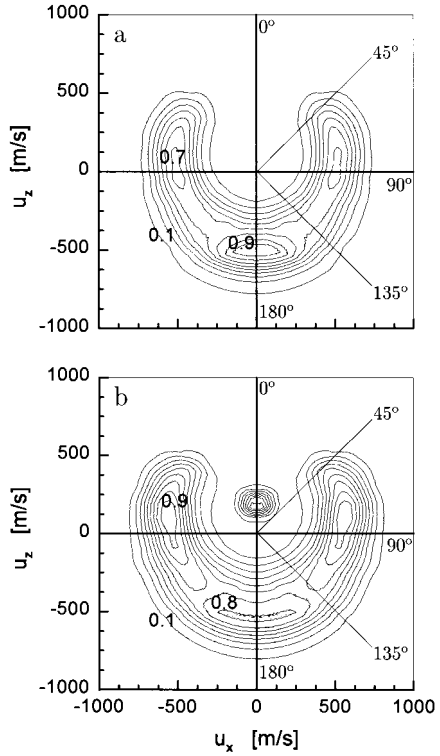

Figure 5. Polar diagram of the double-differential reaction cross section for R1 (panel a) and R2 (panel b). The contour maps represent the result of the fixed velocity approximation (FVA) procedure (eq 5). Note the narrow peak for R2 near the origin (panel b).

3 represent the simulations. The nearly perfect agreement with the reactive portion of the data over the entire range of scattering angles verifies the excellent quality of the cross sections gained by the FVA method. Both maps describe topographically a ring-shaped ridge surrounding a point near the origin but shifted somewhat into the positive $\hat{\mathbf{z}}$-direction. The crest extends over a wide angular range with roughly constant height except for weak undulations near $\vartheta = 90°$ (sideways scattering) and 180°

TABLE 3: Energetics (eV)

	E_{tr}	E_{tot}	$\overline{E'_{tr}}$	f_{tr} (%)[b]	$\overline{E'_{int}}$	f_{int} (%)[c]
R1	1.56	2.56	1.09	42	1.47	58
R2	1.54	2.67				
dominant			0.97	36	1.70	64
minor			0.11	4	2.56	96
$K + C_2H_5I$[a]	1.55	2.58	1.10	43	1.48	57
$K + CH_3I$[a]	1.73	2.63	1.14	43	1.49	57

[a] Reference 19. [b] $f_{tr} = \overline{E'_{tr}/E_{tot}}$. [c] $f_{int} = \overline{E'_{int}/E_{tot}}$.

(backward scattering). Starting at the sideways peak the ridge descends steeply towards $\vartheta = 0°$. In other words, the products are essentially scattered into the backward hemisphere of the CM frame with slight preferences for sideways and backward scattering. Very conspicuous is the additional, well-isolated narrow peak above the origin on the map of R2 which occurs with a branching ratio of only 2% (Figure 5b); it reflects the unexpected slow component in the TOF profiles (Figure 3). These products are ejected sharply into the forward direction of the CM frame with a most probable velocity of exactly the spectator stripping velocity[8,14,17] of KI

$$\mathbf{u_{strip}} = (M_K M_R / M_{KI} M)\mathbf{V} \tag{6}$$

where $\mathbf{V} = \mathbf{V_K} - \mathbf{V_{RI}}$ is the (mean) relative velocity, M_X the mass of the indicated particle, and M the total mass. The relevant velocities are given in Table 1.

The nature of the scattered particles responsible for the isolated peak cannot be identified with certainty by our experimental technique since K atoms and alkali-containing compounds are detected with equal efficiency. Besides KI, slow K atoms may be generated by deeply inelastic collisions that lead to high ro-vibrational excitations of the alkyl iodide or to an excitation of the 4^2P state of K which is marginally accessible. Also the formation of the product C_4H_9K is conceivable as is KI from reactions with dimers. However, there is no apparent reason why these processes are inhibited for the analogous reaction R1 and why these particles travel (accidentally) with the stripping velocity of KI formed in R2. Some concern arose from faint I_2 contaminations of the beam because KI products from $K + I_2 \rightarrow KI + I$ traveling exactly with the (higher) stripping velocity of this reaction would indeed accidentally appear in the LAB frame at the same angles and velocities. However, experiments on $K + I_2$ performed under the same conditions[18] indicate that the KI products travel markedly faster than with the relevant stripping velocity and would appear on the map of R2 as a forward peak around $u_z =$ 400 m/s, twice as wide as observed. In summary, we conclude that the isolated, slow forward peak manifests another KI component (stripping component) formed via a second channel of R2.

The mean translational and internal energy of the products deduced from the contour maps are compiled in Table 3. The mean energy available to the products E_{tot} is the sum of the mean translational energy of the reagents E_{tr} and the exoergicity. For the products of R1 and the fast component of R2, roughly 60% of the available energy is channeled into the internal degrees of freedom of the products ($\overline{E'_{int}}$) but a substantial fraction remains in the translational motion ($\overline{E'_{tr}}$). For comparison we have also included the mean energies for two other alkyl iodide reactions[19] that turn out to be very close to those of R1. At thermal collision energies (around 0.1 eV) the energetics are somewhat different; Rulis and Bernstein[2a,b] found that about ≈40% of E_{tot} is converted to internal energy. In sharp contrast to this, the internal product energy of the minor channel of R2 is exceptionally large; the available energy is nearly completely absorbed. The excited degrees of freedom could be rotation and vibration, but as discussed in section V, the excitation of a low lying electronic state of the *t*-butyl product might be possible too.

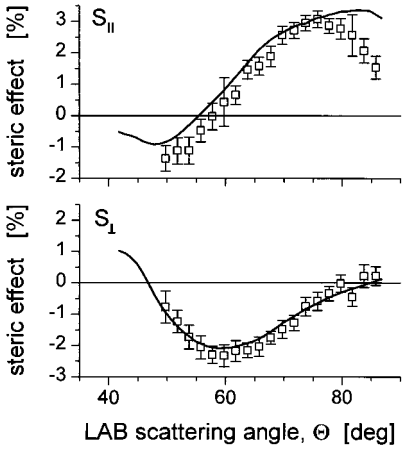

Figure 6. Differential parallel and perpendicular steric effects for R1. The solid lines are the predictions of the DIPR model.

IV. Reactive Scattering from Oriented Molecules

A. Experimental Results. The direction of the orientation field E with respect to the mean relative velocity **V** and scattering plane is described by the polar coordinates β and α as indicated in Figure 4. Basically the flux of scattered particles I_{LAB} is measured as a function of the scattering angle Θ at various field directions, β and α. From these data we extract the differential steric effect

$$S(\Theta, \beta) = \frac{I_{LAB}(\Theta, \beta, \alpha = 0) - I_{LAB}(\Theta, 180° - \beta, \alpha = 180°)}{I_{LAB}(\Theta, \beta, \alpha = 0) + I_{LAB}(\Theta, 180° - \beta, \alpha = 180°)} \tag{7}$$

which is the relative difference of particle flux measured for a pair of opposite field directions. Practically, the detector is positioned to some Θ, and the difference and sum of fluxes are measured by alternating the sign of the voltages applied to the plates of the orientation field. In this way the steric effect becomes widely independent on beam intensity fluctuations $S(\Theta, \beta)$ has been measured as a function of the scattering angle Θ for $\beta = 0$ and 90° denoted by the parallel and perpendicular steric effect, $S_{\parallel}(\Theta)$ and $S_{\perp}(\Theta)$, respectively. If the parallel steric effect is measured, the orientation field E is either parallel or antiparallel to **V**, that is, the K atoms attack preferentially the iodine or the alkyl end of the molecules. Hence $S_{\parallel}(\Theta)$ probes the different probabilities for the ejection of products at Θ of these two collision geometries. The perpendicular steric effect results from two field directions that are perpendicular to **V**. In both situations the K atoms attack the molecules preferentially sideways (perpendicular to the symmetry axis) and create the same total product flux. In this case one would naively expect $S_{\perp} \equiv 0$. On the other hand, if the direction of the ejected products and the direction of the symmetry axis are correlated, $S_{\perp}$ may well be unequal to zero. Hence $S_{\perp}(\Theta)$ is an indicator for the existence of such a correlation.[8]

Parallel and perpendicular steric effects for the reactions R1 and R2 are presented in Figures 6 and 7, respectively. Five points are interesting to notice: (i) R1 and R2 exhibit similar effects with respect to both amplitude and shape. (ii) The

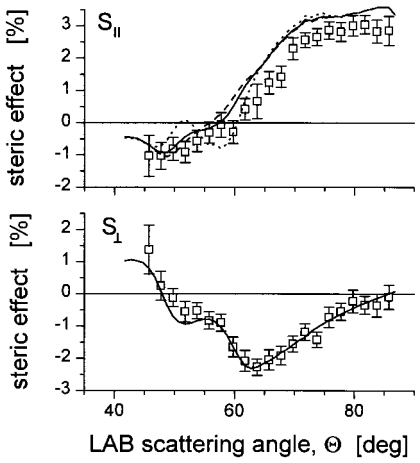

Figure 7. Differential parallel and perpendicular steric effects for R2. The lines are the predictions of the DIPR model. The calculations for $S_{||}$ included the minor component with different weights (a^m): $a^m = 0$ (dashed line), $a^m = -1.0$ (dotted line), and $a^m = -0.25$ (solid line). $S_\perp$ has been calculated only for $a^m = -0.25$.

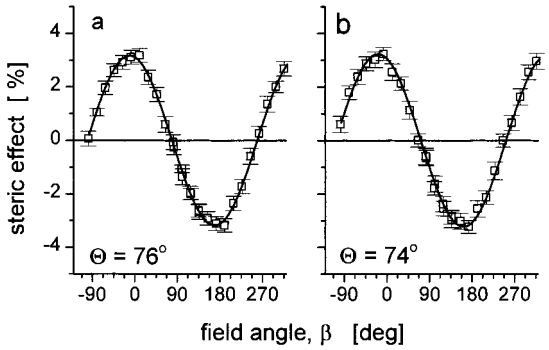

Figure 8. Dependence of the steric effect on the field angle β measured at the indicated LAB angles for R1 (left panel a) and R2 (right panel b). The solid lines are best fit simulations with $A_0 = 0.038$ (R1) and $A_0 = 0.041$ (R2). The purely sinusoidal shape is experimental evidence for the linear cos θ dependence of the calculated axis distribution, eq 2.

apparent magnitude of the effect is small (around 3%) but this is a consequence of the minuscule experimental net orientation. The real size is substantial and close to the theoretical upper boundary (see below). (iii) $S_{||}$ is positive within the angular domain of the most intense product flux. This implies that attacks to the I end are most favorable for product formation. With decreasing angle the effect declines, passes a zero, and becomes negative in the angular range of forward scattering. Obviously, the alkyl end is favorable for the formation of forward scattered products. (iv) $S_\perp$ deviates from zero quite substantially which is considered as evidence for the existence of a correlation between the directions of the main product flux and the molecular symmetry axis. The sign of the effect indicates that more products travel parallel to the axis (from C to I) than antiparallel. (v) The additional slow component of the reaction R2 leads to an inferior structure in the steric effects. The dependence of the steric effect on the field angle β is shown in Figure 8; the indicated scattering angles are located in the regions of maximal product flux. Amplitudes and the sinusoidal shape of the curves contain no significant dynamical information but reflect to a great extent the prepared axis distribution (see following section IV.B).

B. Data Analysis. We describe the orientation-dependent reactive scattering in the CM frame in terms of the orientation-dependent double-differential reaction cross section[13] $I(\cos\gamma_a, \phi_a; \vartheta, \varphi, u)$ where γ_a, ϕ_a denote the polar coordinates of the symmetry axis $\hat{\mathbf{a}}$ in the CM frame (Figure 4). γ_a characterizes the collision geometry and is frequently labeled as *angle of attack*. The differential cross section observable for a certain direction (β, α) of the orientation field E is then an average of I over the prepared axis distribution. On the basis of eq 2 one finds for the average[13]

$$J(\vartheta, \varphi, u; \beta, \alpha) = J_{00}(\vartheta, u) - A_0/3\,[J_{10}(\vartheta, u)\cos\beta + J_{11}(\vartheta, u)\cos(\varphi - \alpha)\sin\beta] \quad (8)$$

where J_{00} is the cross section for the scattering from nonoriented molecules (section III). The cross section like functions J_{10} and J_{11} are the first moments of an expansion of I in a series of real spherical harmonics of the arguments cos γ_a, ϕ_a. These quantities contain the orientational information accessible in the present experiment. The determination of higher moments would require an axis distribution incorporating higher powers of cos θ.

It should be noted that, in principle, three Euler angles are required to define the orientation of the molecule completely. However, the axis distributions of a symmetric or a slightly asymmetric[15] top are exactly or essentially independent of the Euler angle χ_a and thus $I(\cos\gamma_a, \phi_a; \vartheta, \varphi, u)$ can be considered as an average of the orientation-dependent cross section over a uniform χ_a distribution. The situation changes if the asymmetry of the top grows. Then the axis distribution will become χ_a-dependent and the angle must be included in the list of arguments. This more complex situation has been treated recently by Busalla and Blum.[20]

Replacing J_{00} in eq 4 by $J(\vartheta, \varphi, u; \beta, \alpha)$ of eq 8 and inserting the resulting LAB quantities into eq 7 one obtains the following direct relations between the moments and the steric effects:

$$S_{||}(\Theta) = -\,{}^1/_3 A_0 \langle\langle J_{10}(\vartheta, u)\rangle_{\Theta,t}\rangle / I_{LAB}(\Theta) \quad (9)$$

$$S_\perp(\Theta) = -\,{}^1/_3 A_0 \langle\langle J_{11}(\vartheta, u)\rangle_{\Theta,t}\rangle / I_{LAB}(\Theta) \quad (10)$$

The outer bracket $\langle ... \rangle$ symbolizes integration over the time-of-flight t of the products. The sum of the two observed intensities in the denominator of eq 7 has been replaced by $2I_{LAB}(\Theta)$. The integrals in the numerator of eqs 10 and 11 are multiplied by the scaling constant K from eq 4 to be consistent with the experimental quantity in the denominator. The steric effect as a function of Θ and the field angle β is eventually given by

$$S(\Theta, \beta) = S_{||}(\Theta)\cos\beta + S_\perp(\Theta)\sin\beta \quad (11)$$

The sinusoidal β dependence of S is a direct consequence of the linear cos θ dependence of eq 2 employed for averaging I over the axis distribution and reflects no dynamical information.

Following our previous work on iodobenzene[8] and ICl[14] we determine the moments J_{10} and J_{11} by using analytic expressions derived from the DIPR model rather than by fitting the parameters of trial functions to the data. In addition, we employ again a coordinate frame that is parallel to the usual CM frame but moves relative to the latter with the constant stripping velocity (the O frame[8,14]). The relation between scattering angle and recoil velocity in the O and CM frame, γ, w and ϑ, u, respectively, is sketched in Figure 9 (the azimuthal angle φ is the same in both frames). The cross sections and moments in the O frame, denoted by I_{nk}, are related to the corresponding quantities in the CM frame via

$$I_{nk}(\gamma, w)/w^2 = J_{nk}(\vartheta, u)/u^2 \quad (12)$$

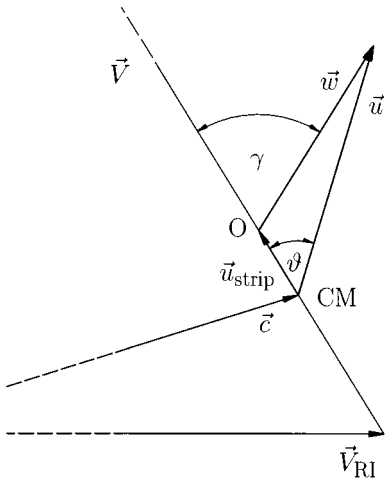

Figure 9. Section of the Newton diagram illustrating the relation between the scattering angle and velocity of products in the O frame γ, **w** and the corresponding quantities ϑ, **u** in the CM frame. $\mathbf{u}_{\mathbf{strip}}$ is the spectator stripping velocity of KI defined by eq 6.

The DIPR expressions for the moments are given by[8,13,14]

$$I^{i}_{10}(\gamma, w) = 3 I^{i}_{00}(\gamma, w) \cos\gamma \tag{13}$$

$$I^{i}_{11}(\gamma, w) = 3 I^{i}_{00}(\gamma, w) \sin\gamma \tag{14}$$

The index i is relevant only for R2 where a minor (i = m) and a dominant (i = d) component are present; then the moments are given by corresponding sums. For the simulation of the steric effects (eqs 9 and 10) we use $J_{nk} = J^{\rm d}_{nk} + a^{\rm m} \cdot J^{\rm m}_{nk}$, where the parameter a^m has been introduced to adjust size and sign of the steric effects of the minor component. The cross sections I^{i}_{00} in eqs 13 and 14 are replaced by $I_{\rm FVA}$(R1) or by the isolated components $I^{\rm d}_{\rm FVA}$ and $I^{\rm m}_{\rm FVA}$(R2) derived from Figure 5, a or b, respectively.

The simulation of the field angle dependence of the steric effect is depicted as a solid line in Figure 8. The excellent fit confirms the sinusoidal shape of the data and thus the linear cos θ dependence of the computed axis distribution eq 2. The correct simulation of the amplitude has been achieved by an adjustment of the orientation parameter A_0; one obtains A_0 = 0.038 and 0.041 for R1 and R2. These values represent lower boundaries for A_0 since the DIPR expressions manifest upper boundaries for the moments.[8] The calculation of axis distributions returns the above orientation parameters for a rotational temperature of $T_{\rm rot}$ = 20 K. Higher temperatures would furnish smaller A_0 values and thus $T_{\rm rot}$ = 20 K turns out to be an upper boundary. Markedly smaller temperatures can be excluded because higher powers of cos θ would become significant and distort the purely sinusoidal shape in contradiction to the data.

The simulations of the differential steric effects are presented in Figures 6 and 7. The data are well rationalized (the above values for A_0 have been used), and considering the simplicity of the model and the complexity of the systems, this is a surprising result. Obviously, the DIPR model describes correctly important aspects of the dynamics of the reactive encounter. The simulation of $S_{\|}$ for R2 includes the dominant and the minor component where the relative weight of the latter is controlled by the factor $a^{\rm m}$. The solid line in Figure 7 is obtained with $a^{\rm m} = -0.25$; neglect of the minor component ($a^{\rm m} = 0$, dashed line) or inclusion with $a^{\rm m} = -1$ (dotted line) deteriorates the fit. This suggests the existence of a steric effect also of the minor component. It is opposite in sign and substantially smaller than the one of the dominant component.

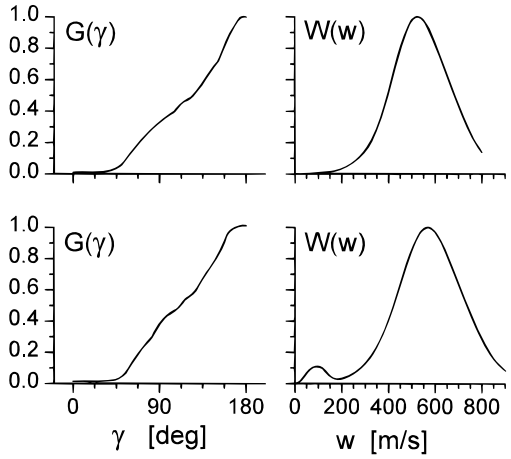

Figure 10. Angular and velocity distribution of products in the O frame: R1 (upper panel), dominant component of R2 (lower panel).

A minor departure of the simulations from the observed steric effects occurs at large angles. The DIPR expression cannot account for the decrease of the effect which is particularly marked for R1. Likely reasons are insufficiencies of the model, e.g., the interaction between the separating products or reorientations of the reagent molecule might become important for the backward scattering and must be considered. Another reason could be deeply inelastic scattered K atoms which would be automatically included in $I_{\rm FVA}$. For a proper simulation of the steric effects the nonreactive contribution has to be extracted from $I^{i}_{\rm FVA}$ in eqs 13 and 14, and the effect would decrease wherever the K flux is present. As mentioned before, there is no experimental indication for such a contribution; however, it cannot be excluded completely. If it is present, the DIPR model would fit the reactive part of the data even better.[19]

In the O frame the product velocity distributions prove to be essentially independent of γ, and hence the cross section factorizes in γ- and w-dependent factors

$$I_{\rm FVA}(\gamma, w) = G(\gamma)\, W(w) \tag{15}$$

This simplified parametrization is of particular importance if a determination of the cross section via a trial and error procedure is attempted (c.f. ref 8). The angular distributions $G(\gamma)$ obtained for R1 and the dominant component of R2 are presented in Figure 10. Both curves indicate pronounced backward scattering without any trace of the preferred sideways scattering observed in the CM frame. For comparison it should be mentioned that we found similar shapes also for the analogous systems[19] K + C_2H_5I and CH_3I and for C_6H_5I[8]. Thus the O frame reveals a close relationship of the dynamics of these reactions although their signature in the CM frame is quite different.

V. Discussion

The crucial assumptions of the DIPR model,[8,13,14] namely (i) the neglect of a reorientation of the target molecule during the approach of the atom, (ii) the impulsive dissociation of the molecular reagent along the symmetry axis $\hat{\mathbf{a}}$, and (iii) the neglect of an interaction between the separating products, lead to the vector relation

$$\mathbf{u} = \mathbf{u}_{\mathbf{strip}} + w \cdot \hat{\mathbf{a}} \tag{16}$$

Equation 16 implies that, given a fixed direction of the symmetry axis, the product molecules in question travel in the O frame with the velocity w into a common direction $\hat{\mathbf{a}}$. In the CM frame a narrow directional distribution of the products results, but nevertheless a tight correlation between the direction of the main

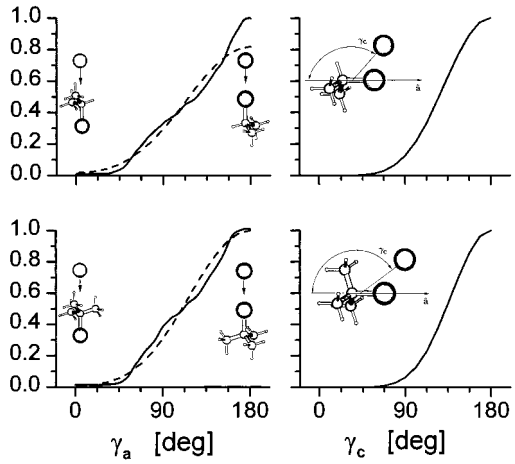

Figure 11. Orientation-dependent integral reaction cross section $G(\gamma_a)$ (on the left) and steric opacity function $P_{st}(\cos\gamma_c)$ (on the right) for R1 (upper panel) and the dominant component of R2 (lower panel). In both reactions KI is favorably formed if the K atoms attack the I end; the reactions are inhibited if K approaches the alkyl end. The dashed lines are best fit simulations based on the opacity functions shown on the right. The half-angle of the cone of nonreaction defined by $P_{st} \leq 0.1$ amounts to 84° (R1) and 93° (R2).

product flux and **â** is still preserved. Our experimental results strongly support the validity of eq 16: First, the existence of a significant perpendicular steric effect is consistent with the tight **u**−**â** correlation predicted by eq 16. Second, eq 16 has been used explicitely to transform the data into the O frame which provided a simple description of the scattering and allowed a unified interpretation of the results. Third, the moments eqs 13 and 14 follow directly from eq 16 and furnish (nearly) quantitative simulations of the observed steric effects. In summary, we conclude that the above-mentioned assumptions are valid to a large extent and play a key role in the dynamics of the considered reactions.

Equation 16 allows easy access to further detailed information on the dynamics[8,14] of the reactions. The velocity w reflects the repulsive energy R released during the explosion of the reagent molecule. Using the velocity distributions $W(w)$ and the relation

$$w = (2R\, M_{alkyl}/M_{KI}M)^{1/2} \qquad (17)$$

we obtain a mean value of $\bar{R} \approx 1$ eV. Furthermore, for a given orientation γ_a, ϕ_a of the symmetry axis all molecules are scattered in the O frame by $\gamma \equiv \gamma_a$ and $\varphi \equiv \phi_a$, and hence, the scattering intensity $G(\gamma)$ is proportional to the orientation-dependent integral reaction cross section $G(\gamma_a)$ (we omit here a new symbol). With the assumption of straight trajectories of the approaching reagents and a spherical reaction shell with radius R_c, $G(\gamma_a)$ can be expressed in terms of the steric opacity function $P_{st}(b, \cos\gamma_c)$[8]. The latter gives the reaction probability of a K atom that encounters the shell with impact parameter b at an angle γ_c between the axis and the line connecting the centers of the molecule and the atom. Using the simple ansatz

$$P_{st}(b, \cos\gamma_c) = \begin{cases} ((1-\cos\gamma_c)/2)^{\lambda} & 0 \leq b \leq R_c \\ 0 & \text{elsewhere} \end{cases} \qquad (18)$$

we could recover $G(\gamma_a)$ fairly well. The fits are given as dashed lines in Figure 11 (on the left); the best fit parameters are $\lambda =$ 3 and 4 for R1 and R2, respectively. The reaction cross section is negligible below $\gamma_a = 30°$ but rises rapidly with the angle and becomes maximal at 180° when the K atoms attack the molecule from the iodine end. Apparently, the alkyl end of the molecules shields the I atom effectively. The steric opacity functions are depicted in the right panel of Figure 11. They define a half-angle of the cone of nonreaction ($P_{st} \leq 10\%$) of 84° and 93° for R1 and R2, respectively. Obviously, the *t*-butyl group represents a more marked hindrance for the reaction than the *i*-propyl group in accord with chemical intuition.

A property common to K + C_6H_5I, ICl, and R2 is the appearance of two product components, a slow and a fast one. The rationale of this phenomenon not observed before at thermal collision energies requires only a minor extension[8,14] of the famous harpooning mechanism[1c] usually invoked to rationalize reactions with alkali atoms. In the case of K + ICl, one has to include a low lying electronically excited state of ICl^- in addition to the ground state such that the migrating (jumping) valence electron of K may select from two rather than from one state only. Subsequent to the jump the anion dissociates to the ground states of the fragments Cl^- and I with different energy release depending on the occupied state. The faster Cl^- forms with K^+, the fast component featuring the tight **â**−**u** vector correlation while the hardly separating fragments lead to the slow stripping component.[14] For K + C_6H_5I it was postulated that the jumping electron may occupy either one of the two states of the anion that dissociate to different (excited) states of the fragments. During the dissociation of $(C_6H_5I^-)^*$ the electron migrates to the repulsive ground state, and both an energetic and a soft dissociation into C_6H_5 and I^- results as required for the two components.

Although ICl, C_6H_5I, and *t*-C_4H_9I feature similar dynamical properties, their electronic structures differ quite significantly. In contrast to this the electronic structures of the alkyl iodides are very similar, but R1 and R2 feature different dynamics. In the following we attempt to develop a rationale for the spectacular difference between R2 and R1 within the framework of the harpooning mechanism. We start the discussion with K + CH_3I, the most simple and best known alkali−alkyl iodide reaction for which only one component has been observed so far. Subsequently we consider the differences in the electronic structure of the target molecules introduced by substituting H atoms with methyl groups and their impact on the reaction.

A schematic diagram of molecular orbital (MO) energies for CH_3I is given in Figure 12. The highest occupied molecular orbital (HOMO) is the nonbonding e($5p_I$) MO localized in the I atom. Below are the σ-type a_1 MO, which causes most of the C-I bond, and the nonbonding e(me) MO localized in the methyl group.[21] The lowest unoccupied MO is the antibonding σ^*-type a_1 MO whose energy steeply increases with decreasing C−I distance.[22] As pointed out by Herschbach[1c] the reaction K + $CH_3I \rightarrow$ KI + CH_3 proceeds in the following way: at the critical distance between the reagents the valence electron of the K atom jumps to the methyl iodide and occupies the antibonding σ^* MO. The potential energy curve of the anion's C−I bond is strongly repulsive, and the anion dissociates suddenly along the symmetry axis **â** into the fragments CH_3 and I^-. K^+ and I^- form the product which departs from the methyl group with substantial recoil energy.

The substitution of three (or two) H atoms of CH_3I by methyl groups does not alter the role and energetic order of the MOs significantly[21] (see Figure 12); only the loss of C_{3v} symmetry causes for *i*-C_3H_7I a splitting of every e MO into an a′ and an a″ MO. The HOMO is again the e($5p_I$) MO. Below lies the σ MO responsible for the C−I bond and above the antibonding σ^* MO whose occupation leads to a rapid dissociation of the

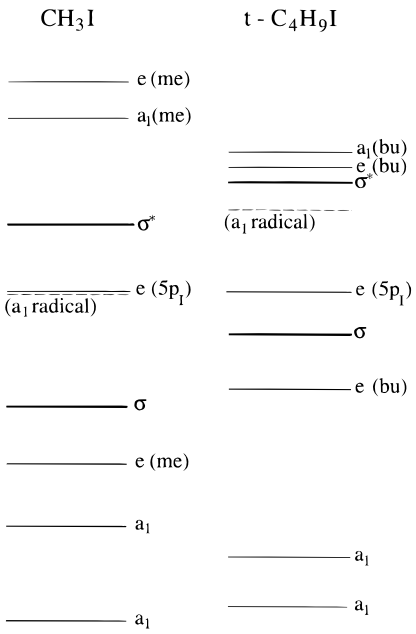

Figure 12. Schematic order of MO energies for CH_3I (left column) and *t*-C_4H_9I (right column). For clarity, the CH_3 groups in *t*-C_4H_9I are considered as quasi atoms. The heavy lines indicate the bonding σ-type and the corresponding antibonding σ^* MOs. The dashed line denotes the HOMO of the methyl or *t*-butyl radical. The HOMO of the alkyl iodides is the e($5p_I$) MO. The highest e, a_1 MOs are empty; they are localized in the methyl or *t*-butyl radical as marked.

C−I bond. Thus the same conditions are provided for the formation of the fast component in R1 and R2 (and other K + alkyl iodides) in the same way as in K + CH_3I. Analogous to the systems discussed above, the formation of a second component demands another empty MO which may be occupied by the jumping electron. Available are an a_1(bu) and an e(bu) MO with predominant *t*-butyl (or *i*-propyl) character like that in CH_3I.[22] It appears conceivable that the electron jumps to one of these MOs and, as they are essentially nonbonding, the anion may start dissociating softly into an electronically excited alkyl radical and I^-. K^+ and I^- combine and form the product that moves forward with the stripping velocity as dictated by momentum conservation if interactions between the products are insignificant.

The appearance of an electronically excited alkyl radical is possible only if the excitation energy is below the available energy, and the crucial question is, are there low lying excited states of the alkyl radical products of R1 and R2? To give a plausible answer we consider CH_3 first. The empty MOs correlate in the united atom limit with the 3s and 3p atomic orbitals of the fluorine atom,[23] and hence their energy rises steeply with decreasing C−H distance. They account for the lowest excited Rydberg states of the methyl radical which feature adiabatic excitation energies of 5.74, 6.95, and 7.43 eV for the $^2A_1'(3s)$, $^2E'(3p)$ and $^2A_2''(3p)$ states,[24] respectively. For the *t*-butyl and *i*-propyl radicals, the energy of these MOs must be significantly lower because strength and length of the C−CH_3 bonds are weaker and larger, respectively, than those of the C−H bond. The downshift of the MO energies is qualitatively supported by results from dissociative electron attachment spectroscopy[25] of the iodides. In addition, the energy of the HOMO of the *t*-butyl radical is by roughly 2 eV higher than the one of methyl.[26] The upshift of the HOMO and the downshift of the empty a_1, e MOs bring them closer together energetically and make the existence of low excited states of the alkyl radicals in R1 and R2 very likely.

We conclude now from the observation of a slow stripping component in R2 that the *t*-butyl radical indeed exhibits an excited state which lies below 2.6 eV (see Table 3). Furthermore, we conclude from the absence of such a feature in R1 that the excitation energy of the *i*-propyl radical lies above this value, and the excited state cannot be accessed in our experiment for energy reasons. A rise of the excitation energy due to the substitution of one methyl group by a hydrogen atom appears quite plausible since the replacement of all three groups shifts the lowest excited state to 5.74 eV (see above). Thus the formation of an electronically excited methyl radical in the reaction K + CH_3I is endoergic by 4.84 eV; it is for this reason that this process has not yet been observed.

The steric opacity function (right panel of Figure 11) shows that the products of R1 and the dominant component of R2 are preferentially formed if the K atoms attack the I end of the molecule, that is, electron jumps to the σ^* MO occur with significant probability only for attacks to the I end, and are inhibited for the reversed collision geometry. Moreover, our data indicate a small parallel steric effect in the minor channel of R2 with a sign opposite to the dominant one. This implies that electron jumps to the empty a_1 or e MOs occur preferentially during attacks to the radical end. A plausible reason could be the localization of the empty MOs in the alkyl group. The sharp forward peaking of this component might then be caused by an enhanced reactivity for grazing collisions with molecules whose symmetry axis points into the forward hemisphere. The slowly departing I^- is picked up by K^+, and both particles continue to travel as KI into the forward direction without interacting with the alkyl radical.

Acknowledgment. Support of this work by the Deutsche Forschungsgemeinschaft (SFB 216, P5) is gratefully acknowledged. We thank Dr. J. Bulthuis for calculating the directional axis distributions.

References and Notes

(1) (a) Herschbach, D. R.; Kwei, G. H.; Norris, J. A. *J. Chem. Phys.* **1961**, *34*, 1842. (b) Herschbach, D. R. *Faraday Disc. Chem. Soc.* **1962**, *33*, 149. (c) Herschbach, D. R. *Adv. Chem. Phys.* **1966**, *10*, 319. (d) Kwei, G. H.; Norris, J. A.; Herschbach, D. R. *J. Chem. Phys.* **1970**, *52*, 1317.

(2) (a) Rulis, A. M.; Bernstein, R. B. *J. Chem. Phys.* **1972**, *57*, 5497. (b) Bernstein, R. B.; Rulis, A. M. *Faraday Disc. Chem. Soc.* **1973**, *55*, 293. (c) Gersh, M. E.; Bernstein, R. B. *J. Chem. Phys.* **1972**, *56*, 6131.

(3) (a) Litvak, H. E.; González Ureña, A.; Bernstein, R. B. *J. Chem. Phys.* **1974**, *61*, 4091. (b) González Ureña, A.; Bernstein, R. B. *J. Chem. Phys.* **1974**, *61*, 4101. (c) Rotzoll, G.; Viard, R.; Schügerl, K. *Chem. Phys. Lett.* **1975**, *35*, 353.

(4) (a) Entemann, E. A.; Kwei, G. H. *J. Chem. Phys.* **1971**, *53*, 4879. (b) Sholeen, C. M.; Herm, R. R. *J. Chem. Phys.* **1977**, *65*, 5398.

(5) Kuntz, P. J. *Trans. Faraday Soc.* **1970**, *66*, 2980; *Mol. Phys.* **1972**, *23*, 1035.

(6) Bañares, L.; González Ureña, A. J. *J. Chem. Phys.* **1990**, *93*, 6473.

(7) van Leuken, J. J.; Bulthuis, J.; Stolte, S.; Loesch, H. J. *J. Phys. Chem.* **1995**, *99*, 13582.

(8) Loesch, H. J.; Möller, J. *J. Phys. Chem. A* **1997**, *101*, 7534.

(9) Brooks, P. R. *Science* **1976**, *193*, 11.

(10) Parker, D. H.; Bernstein, R. B. *Annu. Rev. Phys. Chem.* **1989**, *40*, 561.

(11) Bulthuis, J.; van Leuken, J. J.; Stolte, S. *J. Chem. Soc., Faraday Trans.* **1995**, *91*, 205.

(12) (a) Loesch, H. J.; Remscheid, A. *J. Chem. Phys.* **1990**, *93*, 4778. (b) Loesch, H. J.; Remscheid, A. *J. Phys. Chem.* **1991**, *95*, 8194.

(13) Loesch, H. J. *Annu. Rev. Phys. Chem.* **1995**, *46*, 555.

(14) (a) Loesch, H. J.; Möller, J. *J. Chem. Phys.* **1992**, *97*, 9016. (b) Loesch, H. J.; Möller, J. *J. Phys. Chem.* **1993**, *97*, 2158.

(15) Bulthuis, J.; Möller, J.; Loesch, H. J. *J. Phys. Chem. A* **1997**, *101*, 7684.

(16) Bulthuis, J. Private communication, 1998.

(17) (a) Minturn, R. E.; Datz, S.; Becker, R. L. *J. Chem. Phys.* **1966**, *44*, 1149. (b) Wilson, K. R.; Kwei, G. H.; Norris, J. A.; Herm, R. R.; Birely, J. H.; Herschbach, D. R. *J. Chem. Phys.* **1964**, *41*, 1154.

(18) Höbel, O. Diplomarbeit, Universität Bielefeld, Bielefeld, Germany, 1994.
(19) Möller, J. Dissertation, Universität Bielefeld, Bielefeld, Germany, 1997.
(20) Busalla, A.; Blum, K. *J. Phys. Chem A* **1997**, *101*, 7476.
(21) Boschi, R. A. A.; Salahub, D. R. *Can. J. Chem.* **1974**, *52*, 1217.
(22) Robin, M. B. *Can. J. Chem.* **1985**, *63*, 2032.
(23) Herzberg, G. Electronic Spectra and Electronic Structure of Polyatomic Molecules. *Molecular Spectra and Molecular Structure*, Part III; Van Nostrand Reinold: New York, 1966; p 320.
(24) Mebel, A. M.; Lin, S.-H. *Chem. Phys.* **1997**, *215*, 329.
(25) Modelli, A.; Scagnolari, F.; Distefano, G.; Guerra, M.; Jones, D. *Chem. Phys.* **1990**, *145*, 89.
(26) Koenig, T.; Balle, T.; Snell, W. *J. Am. Chem. Soc.* **1975**, *97*, 662.
(27) Groner, P.; Li, Y. S.; Durig, J. R. *J. Mol. Spectrosc.* **1978**, *72*, 20.
(28) Xu, Q.-X.; Jung, K.-H.; Bernstein, R. B. *J. Chem. Phys.* **1988**, *89*, 2099.
(29) Winkle, W.; Hartmann, H. *Z. Naturforsch.* **1970**, *25a*, 840.
(30) McClellan, A. L. *Tables of Experimental Dipole Moments*; W. H. Freeman and Company: San Francisco, 1963.
(31) *CRC Handbook of Chemistry and Physics*, 55th ed.; West, R. C., Ed.; CRC Press: Cleveland, OH 1975.
(32) Su, T.-M. R.; Riley, S. J. *J. Chem. Phys.* **1979**, *71*, 3194.
(33) The parameters $\bar{\omega} = d|E|/\bar{C}_0$ is typical for the electric interaction energy: $\bar{C}_0 = 0.5(B_0 + C_0)$ denotes the mean rotational constant for rotations perpendicular to the symmetry axis.